Spinel nanoparticles on stick-like Freudenbergite nanocomposites as effective smart-removal photocatalysts for the degradation of organic pollutants under visible light

Spinel nanoparticles on stick-like Freudenbergite nanocomposites as effective smart-removal photocatalysts for the degradation of organic pollutants under visible light

Radu-George Ciocarlan [a, *], Elena M. Seftel [b], Raluca Gavrila [c], Mirela Suchea [c, d], Maria Batuk [e], Myrjam Mertens [b], Joke Hadermann [e], Pegie Cool [a]

[a] LADCA, University of Antwerp (CDE), Universiteitsplein 1, 2610, Wilrijk, Antwerp, Belgium
[b] VITO Flemish Institute for Technological Research, Boeretang 200, B-2400, Belgium
[c] National Institute for Research and Development in Microtechnologies (IMT-Bucharest), 126 A, Erou Iancu Nicolae Street, P.O. Box 38-160, 023573, Bucharest, Romania
[d] Center of Materials Technology and Photonics, Hellenic Mediterranean University, Heraklion, Crete, Greece
[e] EMAT, University of Antwerp, Groenenborgerlaan 171, Antwerp, 2020, Belgium

A B S T R A C T

A series of mixed nanocomposite materials was synthetized, containing a Ferrite phase type $Zn_{1-x}Ni_xFe_2O_4$ and a Freudenbergite phase type $Na_2Fe_2Ti_6O_{16}$, where x = 0; 0.2; 0.4; 0.6; 0.8; 1. The choice for this combination is based on the good adsorption properties of Freudenbergite for dye molecules, and the small bandgap energy of Ferrite spinel, allowing activation of the catalysts under visible light irra-diation. A two steps synthesis protocol was used to obtain the smart-removal nanocomposites. Firstly, the spinel structure was obtained via the co-precipitation route followed by the addition of the Ti-source and formation of the Freudenbergite system. The role of cations on the formation mechanism and an interesting interchange of cations between spinel and Freudenbergite structures was clarified by a TEM-study. Part of the Ti^{4+} penetrated the spinel structure and, at the same time, part of the Fe^{3+} formed the Freudenbergite system. The photocatalytic activity was studied under visible light, reaching for the best catalysts a 67% and 40% mineralization degree for methylene blue and rhodamine 6G respectively, after 6 h of irradiation. In the same conditions, the well-known commercial P25 (Degussa) managed to mineralize only 12% and 3% of methylene blue and rhodamine 6G, respectively. Due to the remarkable magnetic properties of Ferrites, a convenient recovery and reuse of the catalysts is possible after the photocatalytic tests. Based on the excellent catalytic performance of the nanocomposites under visible light and their ease of separation out of the solution after the catalytic reaction, the newly developed composite catalysts are considered very effective for wastewater treatment.

1. Introduction

Over the past decades, industry expanded considerably in many directions, including the textile industry, a well-known sector for the production of an enormous amount of wastewater. For this reason, a number of possible water treatment technologies have been developed over the years, such as advanced oxidation processes (AOPs) [1–3], biological methods [4], membrane systems [5], adsorption approaches [6,7], *etc.* in order to maintain the ratio between the drinking water and wastewater. Among those technologies, advanced oxidation processes (AOPs) are receiving a lot of attention due to the numerous materials able to sustain photocatalytic reactions [8,9].

In photocatalytic processes, light is used to generate electron (e^-)-hole (h^+) pairs in semiconductor materials, by promoting the electrons from the valence band (VB) to the conduction band (CB) [10]. Although the results are promising, the most important limitations to address remain: large band-gap energy required to activate some catalysts, recombination rate between e^--h^+ pairs which leads to the inactivation of the catalysts and difficulty to recover the catalysts after their use [11,12]. Many studies have been

* Corresponding author.
E-mail address: radu-george.ciocarlan@uantwerpen.be (R.-G. Ciocarlan).

focused on photocatalytic reactions in the presence of simple oxides *e.g.* TiO_2 [10,13–15], ZnO [16], Fe_2O_3 [17], WO_3 [18], SnO_2 [19] *etc.*, in order to degrade organic pollutants. Other researchers have concentrated their work on mixed oxide materials *e.g.* spinel [20,21], perovskite [22,23] and ilmenite [23,24] structures, as semiconductors in photocatalytic reactions.

A special case, enclosed in the group of spinel structures, is represented by the Ferrites, following the general formula MFe_2O_4. Well-known for their magnetic and electric properties, Ferrites represent a promising candidate for the use in photocatalytic applications, due to their narrow band-gap energy (~2 eV) [25], chemical stability, synthesis versatility and strong magnetic properties, which represent an advantage for the recovery process [26]. More specifically, $ZnFe_2O_4$ and $NiFe_2O_4$ have been highlighted as having good photocatalytic properties, with a band-gap energy of 1.92 eV [25] respectively 2.33 eV [27]. Previous studies showed remarkable photocatalytic properties in nanocomposite materials containing $ZnFe_2O_4$ *e.g.* $ZnFe_2O_4/TiO_2$, $TiO_2/ZnFe_2O_4$, $Co_3O_4/ZnFe_2O_4$, $ZnO/ZnFe_2O_4$, $Fe_2O_3/ZnFe_2O_4$, RGO/$ZnFe_2O_4$, CNTs/$ZnFe_2O_4$, Ag/ZnO/$ZnFe_2O_4$, CMSs@$ZnFe_2O_4/Ag_3PO_4$, ZnO/$ZnFe_2O_4$@carbon nanospheres [28]. At the same time, $NiFe_2O_4$ has been used in photocatalytic processes, as part of the nanocomposites such as $NiFe_2O_4$/ZnO [29], $NiFe_2O_4/Bi_2O_3$ [30], $NiFe_2O_4$@TiO_2 [31], Au/g-$C_3N_4/NiFe_2O_4$ [32], $Ag_3PO_4/NiFe_2O_4$ [33].

Another material with notable adsorption and magnetic properties is Freudenbergite ($Na_2Fe_2Ti_6O_{16}$), described by Frenzel and McKie in 1961 respectively 1963, before the structure was clarified by Ishiguro et al. in 1978 [34]. The Freudenbergite structure presents many similarities with the titanate-like structures, being included in their class of materials [35]. Guo et al. obtained magnetic Freudenbergite plate-like structures, via the hydrothermal method, with double edges in the visible light domain (2.2 eV and 2.53 eV) for the efficient removal of methylene blue dye [36]. Previous studies showed excellent results for the use as safety storing radioactive waste materials, known as "synroc" materials [37,38]. In the Freudenbergite structure, Na^+ ions are found in the tunnel cavities formed by Ti^{4+}/Fe^{3+} octahedrons, allowing a good absorption of waste materials and a low leaching level.

Hereby we report on the synthesis, characterization and photocatalytic activity testing of a mixed system consisting of Zn–Ni Ferrite and Freudenbergite. Previous studies showed a synergistic effect between Zn^{2+} and Ni^{2+} in spinel structures, for the degradation of methyl orange and methylene blue, thus leading to the extended study of the Ni–Zn Ferrite system [39]. The aim is to design a novel Zn–Ni combination of cations into a Ferrite/Freudenbergite nanocomposite which may offer the advantage of using the remarkable catalytic properties of Zn^{2+} together with the strong magnetic properties of Ni^{2+} in the spinel-type structure. The photocatalytic activity is studied for the mineralization of two model dyes, *e.g.* methylene blue and rhodamine 6G, under visible light irradiation, and compared with the P25 (Degussa) commercially available reference photocatalyst.

2. Experimental

In order to obtain the nanocatalysts we used a two-step synthesis procedure, followed by the calcination at 500 °C for 6 h to crystallize the phases. Firstly, the Zn–Ni Ferrites were obtained via the co-precipitation route by mixing solutions of 0.2 M $Zn(NO_3)_2$•$6H_2O$, 0.2 M $Ni(NO_3)_2$•$6H_2O$ and 0.4 M $Fe(NO_3)_3$•$9H_2O$. The general formula of the obtained Ferrites is $Zn_{1-x}Ni_xFe_2O_4$, where x is alternatively 0; 0.2; 0.4; 0.6; 0.8 and 1. After 1 h of stirring at 80 °C, the precipitation agent was added (3 M NaOH) until a pH between 12 and 13 was reached and the mixture was further stirred for another 1 h. Secondly, the Ti-source source (titanium butoxide denoted as TBOT) was added and the solution was vigorously stirred for 16 h at 60 °C. The ratio between $Zn_{1-x}Ni_xFe_2O_4$:TBOT was 1:5 (wt %), considering the density of TBOT as 1 g/mL at 20 °C. Finally, the product was filtrated and washed several times with water and ethanol, dried and calcined at 500 °C in air for 6 h. For simplicity, in the following sections the as-prepared samples will be denoted $Zn_{1-x}Ni_xFe_2O_4$–$Na_2Fe_2Ti_6O_{16}$ (where x = 0; 0.2; 0.4; 0.6; 0.8 and 1).

The photocatalytic tests were performed under visible light irradiation, in a reactor equipped with a cooling system in order to maintain a constant temperature during irradiation. The ratio between catalysts and dyes' solutions was 0.5 g/L. In a typical experiment, 25 mg of catalyst were mixed with 50 ml of dye solution. The beginning part of the experiment was performed in dark (the lamp was off) for an appropriate time interval, to reach adsorption equilibrium of the dye on the catalysts surface (~30 min). After the equilibrium time has been reached, the irradiation with visible light started. At the same time, the concentration of dyes' solutions was 4×10^{-5} M, prepared in Milli-Q water.

3. Characterization techniques

The structural characterizations include X-ray powder diffraction (XRD), Raman spectroscopy and UV–vis diffuse reflectance spectroscopy (UV–Vis DR). To verify and resolve the structure and morphology of the samples, transmission electron microscopy (TEM) and N_2-sorption measurements were used. To follow the degradation of the dyes during the photocatalytic tests, UV–Vis spectroscopic measurements and total organic carbon (TOC) analyses were used.

The XRD patterns were obtained after the thermal treatment, using a PANalytical X'Pert PRO MPD diffractometer equipped with Cu Kα radiation. The analyses were performed in 2θ mode, with a scanning speed of 0.04°/4 s. Raman spectra were recorded using a Micro-Raman Horiba (Xplora Plus Microscope) equipped with a green 532 nm laser, in the range 50 cm^{-1} to 1000 cm^{-1} raman shift. The UV–Vis DR spectra were collected on a Thermo Nicolet Evolution 500 UV–Vis spectrometer, equipped with a diffuse reflectance accessory and using KBr as reference. The same instrument coupled with liquid phase accessory suitable for the quartz cuvettes was used for the UV–Vis liquid phase measurements. Conventional bright field TEM images and electron diffraction (ED) patterns were acquired on Philips CM20 and FEI Tecnai G2 microscope operated at 200 kV. High angle annular dark field scanning transmission electron microscopy (HAADF-STEM) images and energy dispersive X-ray (EDX) maps were acquired on the FEI Titan microscope equipped with a Super-X detector and operated at 300 kV. To prepare the specimen for TEM analysis, the material was grinded in ethanol. A few drops of the obtained suspensions were deposited onto a Cu TEM grid covered with carbon. Na and Zn elementary distribution in the analyzed samples was not possible to collect since Na–K and Zn-L lines are very close (1.04 and 1.01 keV, respectively), so their EDX maps cannot be distinguished. Morphological characterization of the crystalline oxides was also performed by Atomic Force Microscopy (AFM) using a Ntegra Aura Scanning Probe Microscope (NT_MDT Spectrum Instruments). AFM scans were performed in Intermittent-contact mode, using a Mikromasch® medium-soft probe (9 N/m nominal force constant). The oxide powders were dispersed in IPA and the resulted solution was sonicated for 5 min. Next the supernatant was drop casted onto a crystalline silicon substrate and allowed to dry. Surface area data were obtained on a Quantachrome Quadrasorb SI (Quantachrome Instruments, Odelzhausen, Germany) using N_2 as adsorbate at liquid nitrogen temperature of −196 °C. Before the analyses, the samples were outgassed under vacuum for 16 h and at 200 °C. The TOC analyses

were done using a Shimadzu TOC-VCPH (Shimadzu, Kyoto, Japan) analyzer equipped with a NDIR detector. TOC values were obtained by subtracting IC (inorganic carbon) values from TC (total carbon) values. For the photocatalytic experiments, the visible light irradiation was generated by a lamp US800 (Sun simulator-UNNASOL Germany, 250W), combined with a blocking filter for the UV light (USF400). For the UV light test, a different filter was used to block the visible light (US11).

4. Results and discussions

The synthesis of the nanocomposites followed a two steps procedure. In the first step, when the NaOH was added, a mixture of three main hydroxides was formed, *e.g.* $Fe(OH)_3$ [40], $Zn(OH)_2$ [41] and $Ni(OH)_2$ [42]. After the addition of the Ti source and the calcination process, part of these hydroxides formed the spinel structure and another part together with Na^+ and Ti^{4+} formed the Freudenbergite structure. A higher concentration of the Ni^{2+} and Zn^{2+} in the spinel structure on the count of the migration of Fe^{3+} towards the formation of the Freudenbergite structure was expected. At the same time, the Fe^{3+} was substituted by Ti^{4+} as proved by the EDX characterization results.

The two steps synthetic approach is schematically illustrated in Fig. 1.

The role of NaOH in the formation mechanism is twofold: firstly, it establishes the alkaline environment necessary for the co-precipitation reaction and the formation of the titanate-like structure. The second key role is its contribution as sodium ions source for the formation of the $Na_2Fe_2Ti_6O_{16}$ structure.

Phase identification and purity information for the series of catalysts were extracted from X-ray diffraction (XRD) measurements. Fig. 2 shows the XRD patterns collected from samples calcined at 500 °C, for 6 h. As it can be observed from the Fig. 2, all reflections in the XRD were exclusively indexed to a spinel structure, with cubic symmetry – space group Fd-3m, respectively to Freudenbergite structure, with monoclinic symmetry – space group C 2/m and confirming the formation of Ferrites and $Na_2Fe_2Ti_6O_{16}$.

In general, 2 sites are found in the spinel structures *e.g.* octahedral (B) and tetrahedral (A) sites, with a specific occupancy of the cations, as shown in Fig. 3A. Depending on the cations sites, 3 types of spinel structure may be formed. In the first case, the divalent cations (M^{2+}) are found on the tetrahedral sites and the trivalent cations (M^{3+}) on the octahedral sites, forming a pure normal spinel structure. In the second case, the divalent cations (M^{2+}) are found on the octahedral sites together with half of trivalent cations (M^{3+}), while the other half of the trivalent cations are found on the tetrahedral sites, assembling a pure inverse spinel structure. Finally, the third case, can be defined as a spinel structure with an inversion degree (mixed normal-inverse spinel), denoted *u*, and representing the fraction of the tetrahedral sites that are occupied by trivalent cations (M^{3+}). Previous studies showed that Zn^{2+} is occupying the tetrahedral sites (normal spinel) and Ni^{2+} is occupying the octahedral sites (inverse spinel), resulting in a mixed normal-inverse structure, which is valid for b-e samples in Fig. 1; Fe^{3+} is more versatile and can be found in both sites [43–45].

Freudenbergite ($Na_2Fe_2Ti_6O_{16}$) was described in previous studies, to have an isostructural ordering with the sodium titanate parental material ($Na_xTi_4O_8$) [46,47]. Similar structure (isostructural) to $Na_2Fe_2Ti_6O_{16}$ was obtained by G. Bruhn et al. by replacing Fe^{3+} with Zn^{2+} and resulting in $Na_xZn_yTi_{8-y}O_{16}$ [47,48]. In a typical Freudenbergite structure, the two octahedral sites are occupied by Fe^{3+} and Ti^{4+}, while each Na^+ site is surrounded by eight O^{2-} ions, as shown in Fig. 3B [34]. Cashion et al., Ishiguro et al. and Chen et al. showed that Fe^{3+} and Ti^{4+} are randomly distributed on the two octahedral sites of the Freudenbergite structure [34,49,50]. It was reported that in many cases the Freudenbergite is obtained as a side phase and very rarely in a pure phase, making it difficult to study [36,51,52].

In the as-prepared nanocomposites, it was observed that increasing the Ni^{2+} and decreasing of Zn^{2+} contents, leads to decreasing of the crystallite size (Table 1) of the spinel structure, except for the $ZnFe_2O_4$–$Na_2Fe_2Ti_6O_{16}$. This decrease of the crystallite size can be correlated with the strong tendency of Ni^{2+} to occupy the octahedral sites of the spinel structure. Another explanation for this decrease can be associated to the different ionic radius and crystal radius in the octahedral symmetry, which were observed to be smaller for Ni^{2+} than for Zn^{2+} (0.69; 0.83 for Ni^{2+} and 0.74; 0.88 for Zn^{2+}) [53]. At the same time, the Ferrite nanoparticles size is relatively small, even after the calcination at 500 °C, as observed in TEM, which would be discussed later. This may be assigned to the migration of the Fe^{3+} cations to form the Freudenbergite system. A small part of the Ti^{4+} was found in the structure of the Ferrites, as the interchange of the cations can occur in both ways, from Ferrite to Freudenbergite and from Freudenbergite to Ferrite. These results were confirmed by EDX measurements on individual Ferrite and Freudenbergite nanoparticles.

Raman spectroscopy was further used to investigate the formation of the Freudenbergite having titanate-like structure together with the spinel structure. The weak bands positions corresponding to spinel structure in the Raman spectra are presented in Fig. 4 and they are encircled. The weak band around 700 cm^{-1}

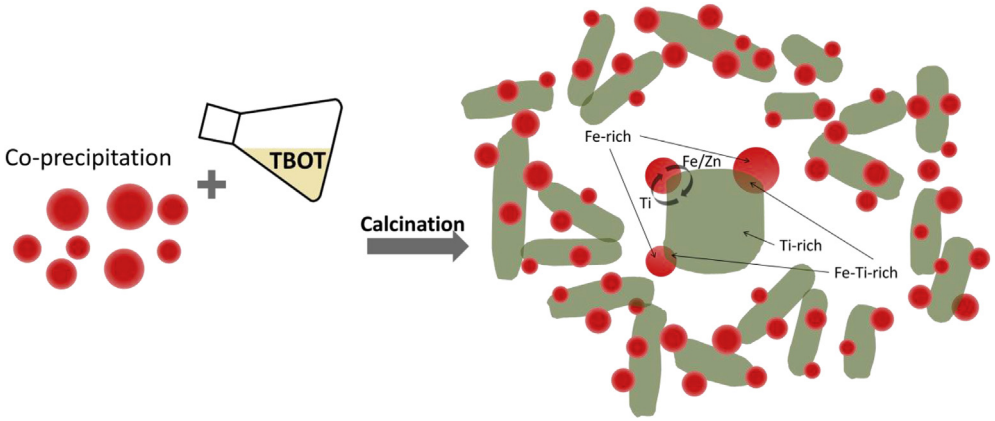

Fig. 1. Schematic representation of the two steps synthesis procedure of $Zn_{1-x}Ni_xFe_2O_4$–$Na_2Fe_2Ti_6O_{16}$ (x = 0; 0.2; 0.4; 0.6; 0.8; 1).

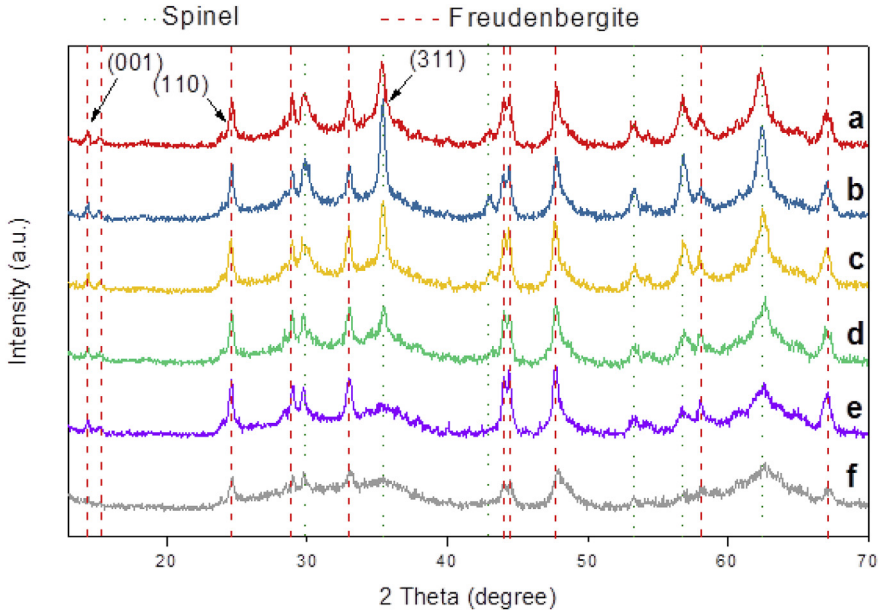

Fig. 2. XRD patterns corresponding to a→f – $Zn_{1-x}Ni_xFe_2O_4$–$Na_2Fe_2Ti_6O_{16}$ (x = 0; 0.2; 0.4; 0.6; 0.8; 1).

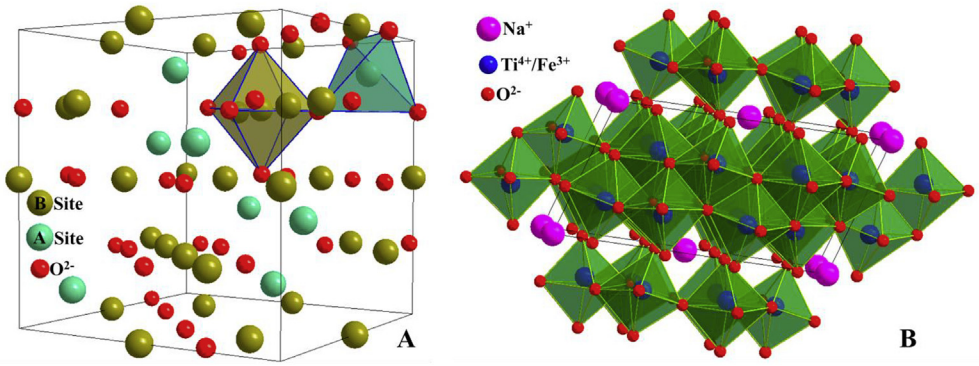

Fig. 3. Crystal structures of A-spinel and B-Freudenbergite.

Table 1
Crystallite size of the Ferrites in each nanocomposite, band-gap energy and surface area of the nanocomposites and P25.

Sample	Crystallite size corresponding to $Zn_{1-x}Ni_xFe_2O_4$ (nm)[a]	Band-gap energy (eV) of the nanocomposites[b]	Surface area (m^2/g) of the nanocomposites[c]
$ZnFe_2O_4$–$Na_2Fe_2Ti_6O_{16}$	12	2.7	22
$Zn_{0.8}Ni_{0.2}Fe_2O_4$ –$Na_2Fe_2Ti_6O_{16}$	18	3.2	23
$Zn_{0.6}Ni_{0.4}Fe_2O_4$ –$Na_2Fe_2Ti_6O_{16}$	15	2.8	20
$Zn_{0.4}Ni_{0.6}Fe_2O_4$ –$Na_2Fe_2Ti_6O_{16}$	10	3.0	20
$Zn_{0.2}Ni_{0.8}Fe_2O_4$ –$Na_2Fe_2Ti_6O_{16}$	5	2.8	21
$NiFe_2O_4$–$Na_2Fe_2Ti_6O_{16}$	5	2.6	25
P25	n.a.	3.3	60

[a] Calculated with Scherrer's equation [54].
[b] Calculated from Tauc's plot [55].
[c] Calculated with BET method [56].

corresponds to the symmetric stretch of MO_4 in tetrahedral sites, shifting to higher values with the increase of the Ni^{2+} content. In case of $ZnFe_2O_4$– $Na_2Fe_2Ti_6O_{16}$ (Fig. 4 a-spectrum), the band present at 641 cm^{-1} consists of two overlapping bands *e.g.* the weak band of pure $ZnFe_2O_4$ and the titanate band. The band of MO_4 in tetrahedral sites for pure $ZnFe_2O_4$ and $NiFe_2O_4$ Ferrites appears at different values, 647 cm^{-1} respectively 700 cm^{-1} (Fig. S1 - see Supporting information) confirming the shift towards higher Raman wavenumber values. The Raman mode around 340 cm^{-1} corresponds to Eg symmetry of the Ferrite and the broad band

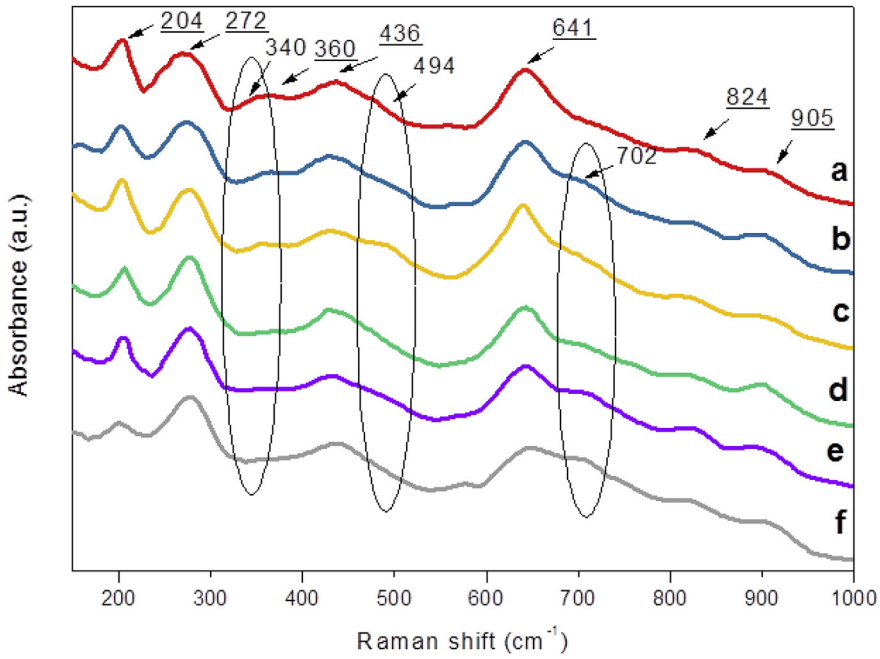

Fig. 4. Raman spectra corresponding to a→f – $Zn_{1-x}Ni_xFe_2O_4$–$Na_2Fe_2Ti_6O_{16}$ (x = 0; 0.2; 0.4; 0.6; 0.8; 1).

around 494 cm^{-1} can be correlated to the vibration of the octahedral site of the Ferrite phase [57].

Most of the titanates features are still in debate when it comes to exact interpretation, due to the different settings of Raman instruments and consequently to the shifts that appear. For monoclinic titanate structures, the spectra cannot be superimposed onto anatase, rutile, brookite or TiO_2(B), but appear closer to the spectra corresponding to titanate nanotubes. In a typical Raman spectrum of a titanate-type material, the well-defined peaks correspond mostly to TiO_6 octahedron, due to the high sensitivity of Ti-oxide structures to Raman spectroscopy. Freudenbergite, similar to sodium titanates, exhibit features around 204, 272, 360, 436, 641, 824 and 905 cm^{-1}. Therefore, the bands centered at 204 and 436 cm^{-1} may be correlated to a Ti–O–Ti vibration framework and the bands centered at 272, 641 cm^{-1} may be assigned to Ti–O-M vibration (M = Na^+, Fe^{3+}). The bands at 824 and 905 cm^{-1} correspond to Ti–OH vibrations respectively Ti–O–Na [40,58,59].

The optical absorption spectra of the nanocomposites and reference material P25 are shown in Fig. 5, while the Tauc plots for the band-gap approximation are represented in Fig. S2 (see Supporting Information). The spectra can be divided in two main regions corresponding to the UV and visible parts of the light spectrum. Freudenbergite, as a special case of titanates with a stick-like structure, exhibits a higher band-gap energy, compared to the anatase or rutile TiO_2-type materials [58]. TiO_2 is one of the most studied materials in photocatalysis, in both, anatase and rutile phases that have the band-gap energy of 3.2 eV and 3.0 eV respectively [41]. In the UV region of the spectrum (<400 nm), the absorption is mainly due to the contribution of Ti–O species, from titanate-like structures.

The second region of the spectra presents the behavior of the photocatalysts in the visible range of light spectrum (~400–800 nm). In visible, a wide absorption band is present for all the nanocomposites, characteristic to the Fe_2O_3, ZnO and NiO presence in the spinel structure. The largest UV-VIS radiation absorption over the whole spectrum (200–800 nm) was observed for the $NiFe_2O_4$–$Na_2Fe_2Ti_6O_{16}$; the lowest absorption in the UV spectral region was observed for $Zn_{0.6}Ni_{0.4}Fe_2O_4$–$Na_2Fe_2Ti_6O_{16}$ and in

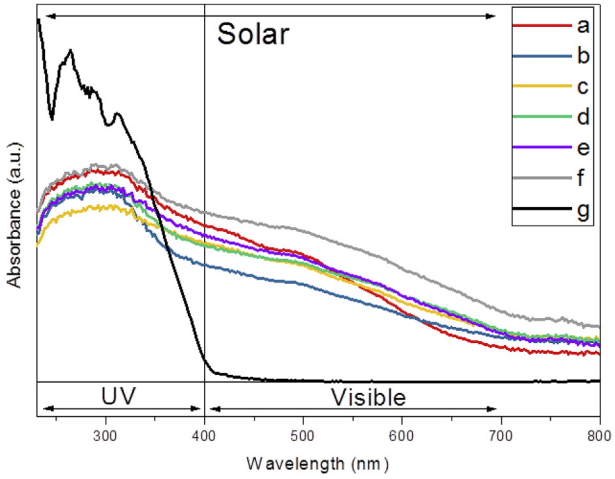

Fig. 5. UV-DR spectra of a→f – $Zn_{1-x}Ni_xFe_2O_4$–$Na_2Fe_2Ti_6O_{16}$ (x = 0; 0.2; 0.4; 0.6; 0.8; 1) and g – P25.

the visible spectral region for $Zn_{0.8}Ni_{0.2}Fe_2O_4$–$Na_2Fe_2Ti_6O_{16}$. The band-gap energies were approximated using the Tauc plots, by representing $(\alpha h\upsilon)^2(eV/cm)^2$ vs. Photon energy (eV) [55]. The values were found to be between 2.6 eV for $NiFe_2O_4$–$Na_2Fe_2Ti_6O_{16}$ and 3.2 eV for $Zn_{0.8}Ni_{0.2}Fe_2O_4$–$Na_2Fe_2Ti_6O_{16}$ (Fig. S2 - see Supporting Information). At the same time, a lower band-gap energy was determined for the nanocomposites containing only Ni-Ferrite and Zn-Ferrite, than that corresponding to the nanocomposites containing the mixed phases. Guo et al. reported that two absorption bands edges may be observed for the Freudenbergite nanosheets [36]. The present samples did not show double absorption bands, presumably due to the large absorption of the Ferrites over the whole UV–Vis spectrum. Furthermore, a large difference in band-gap values may occur in materials with different dimensionalities, even if the materials consist of the same components [40].

The $Zn_{0.8}Ni_{0.2}Fe_2O_4$–$Na_2Fe_2Ti_6O_{16}$ sample was selected for further TEM and EDX analyses, due to its higher crystallinity determined from the XRD patterns. According to the EDX spectra, ED, TEM and HAADF-STEM images, the nanocomposites contain two phases, *e.g.* one Fe-rich with a spinel structure and one Ti-rich with a titanate-like Freudenbergite structure, which may be well correlated with the XRD and Raman observations. The spinel nanoparticles are isometrically shaped as one can see from Fig. 6*a* and *b*, while the Freudenbergite phase shows a needle-like morphology as obvious from Fig. 6*b*. The high resolution TEM image of a Freudenbergite particle is shown in Fig. 6c and demonstrates the presence of the (001) planes having a spacing of 0.62 nm, in agreement with the typical Freudenbergite structure lattice parameters. A close up of the area indicated by a white rectangle is shown in Fig. 6*e*. Fig. 6*f* shows the electron diffraction pattern corresponding to this Freudenbergite particle in the imaged zone. Fig. 6*d* shows a high resolution HAADF-STEM image of a spinel nanoparticle oriented along the [1$\bar{1}$0] direction ([211] is shown in Fig. S3C - see Supporting Information). Fig. 6*h* shows a close up of the indicated area of Fig. 6*d*, with an overlay of the spinel structure, red are marking the Fe-atoms and blue the Zn-atoms. Overview images of the surrounding area of this particle is shown in Fig. S3A and Fig. S3B in the Supporting information. EDX spectra of the three particles presented in Fig. 6*g*–*h* are also shown in the Supporting Information, Figs. S3E–3F and confirm the presence of Fe, Zn and Ni in the spinel nanoparticles, as well as a clear Ti peak, indicating that a small amount of Ti penetrated into the spinel structure. At the same time, part of the Fe diffused into the titanate-like structure to form the Freudenbergite phase (see Fig. S3F - Supporting Information). An EDX map of these particles, including only the elements Fe and Ti, for clarity, is shown in Fig. 6*h* (see also Fig. S3D, corresponding HAADF-STEM in Fig. 6*g*).

The EDX spectra (see Fig. S3E in Supporting Information) corresponding to the three particles shown in Fig. 6*h*, reveal the atomic ratio of Fe, Zn, Ni and Ti to be 57.4/32.7/4.8/5.1 ($Zn_{0.98}Ni_{0.15}Ti_{0.15}$-$Fe_{1.72}O_x$) (blue spectrum) and 59.3/26.3/6.4/8.1 ($Zn_{0.79}Ni_{0.19}Ti_{0.24}$-$Fe_{1.78}O_x$) (red spectrum), for the left and right spinel nanoparticles, respectively. The EDX spectrum of the Freudenbergite particle (see Fig. S3F Supporting Information) gives an atomic ratio of Ti, Na and Fe of 82.5/15.7/1.8. The Na content may be underestimated due to the low energy of the Na peak in the EDX spectrum.

Fig. 7 a and b show in 2D, respectively 3D rendering, the AFM image of a bundle of elongated features (representing the Freudenbergite phase), together with multiple individual particles (identified as Ferrite particles). The elongated features form a dendritic structure, with small filaments about 2.5–3 nm height joining larger branches, two or threefold the size of the filaments. On the other hand, individual Ferrite particles noticeable off the filaments are about the same size. The AFM imaging suggests that the elongated features of Freudenbergite act as a support for the Ferrite nanoparticles, inhibiting the agglomeration (due to their magnetic properties) and increasing the number of active sites.

The nitrogen sorption analysis results are presented in Fig. S4 in Supporting Information, showing characteristic isotherms of type III with a type H3 hysteresis loop [56]. The surface area was found to be between 20 and 25 m^2/g, as shown in Table 1. The porosity of the catalysts can be correlated to the interparticle arrangement and is not due to the intraparticle pores. The behavior is characteristic for inorganic metal oxides, obtained without the use of surfactants or other types of template materials. Compared with the reference material used in photocatalysis P25, the surface area of as-prepared materials is almost 3 times smaller (Fig. S4).

4.1. Photocatalytic results

Three model dyes, namely methylene blue (MB) and rhodamine 6G (R6G) as cationic dyes, and one anionic dye methyl orange (MO), were used to test visible light photodegradation in the presence of

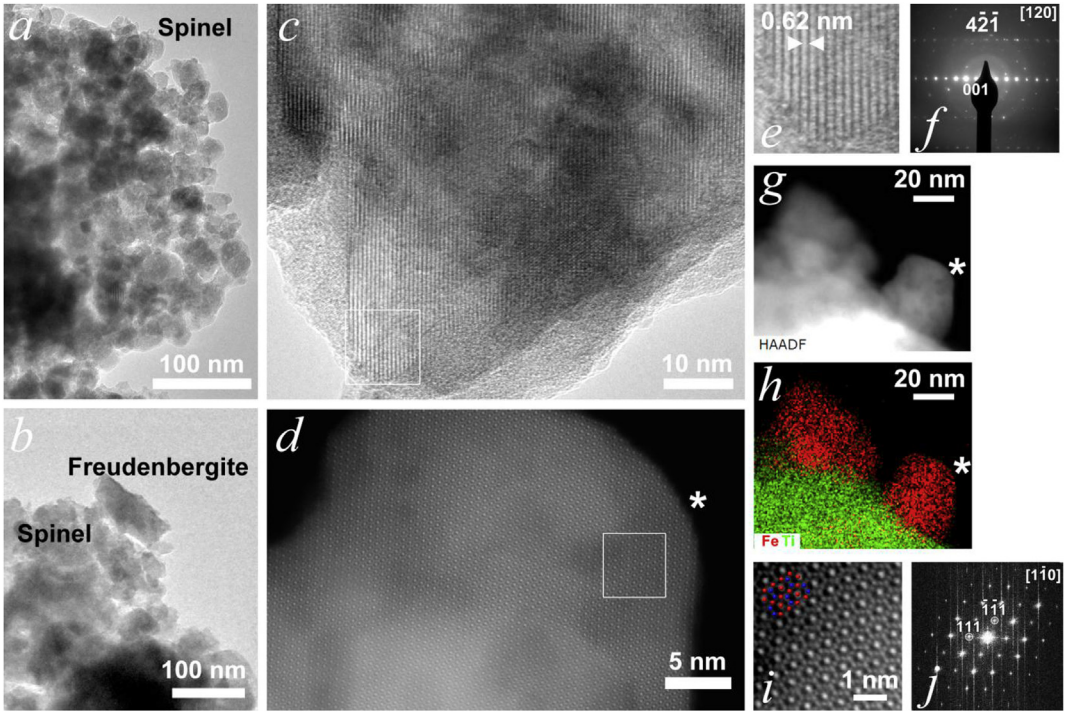

Fig. 6. TEM results on $Zn_{0.8}Ni_{0.2}Fe_2O_4$–$Na_2Fe_2Ti_6O_{16}$. ***a***. TEM overview image of spinel particles; ***b.*** TEM image showing both spinel particles and a Freudenbergite particle; ***c***. high resolution HAADF-STEM image of a Freudenbergite particle; ***d***. high resolution TEM image of a spinel particle; ***e***. enlargement of the area indicated in Fig. ***c***; electron diffraction patterns of the particle in Fig. ***c***; HAADF-STEM and STEM-EDX map of particles including the one in Fig. ***d*** (the star (*) indicates the corresponding position; ***i***. high resolution HAADF-STEM image of the spinel particle indicate by a star in Fig. ***h***; ***i***. close up of the area indicated in Fig. ***d***; Fourier transform of the whole particle shown in Fig. ***d***.

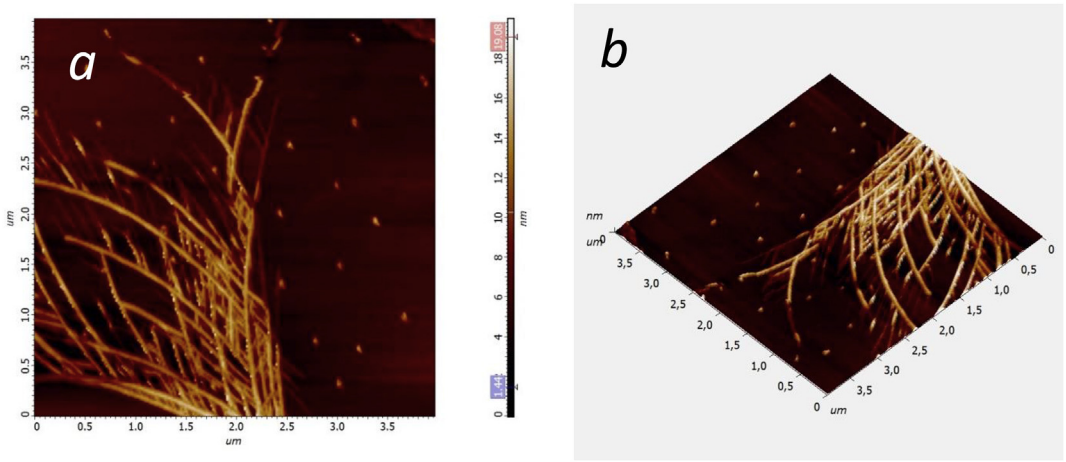

Fig. 7. 4 × 4 μm scan size AFM image of NiFe2O4—Na2Fe2Ti6O16 nanocomposite (a: top view; b: 3D rendering). Z-range: 20 nm.

$ZnFe_2O_4$—$Na_2Fe_2Ti_6O_{16}$, as shown in Fig. 8.

The UV-VIS spectroscopy results show that after 80 min of irradiation, around 50% of the MB, 30% of R6G and 0% of MO were degraded. Note that from the equilibrium times, for the two cationic dyes, namely MB and R6G respectively, a strong interaction with the catalysts was observed, compared to the anionic dye MO, where no interaction occurred. This may be correlated with the synthesis conditions at high pH of the titanate-type materials leading to a negatively charged surface in solution [40]. Moreover, Guo et al. found that the Freudenbergite is negatively charged at pH 6 from Zeta potential measurements, which was the same pH observed for the MO dye solution [36]. As such, stronger interactions occur when the charge of the catalyst and the dye are different, while no interaction occurs when they have similar charges. For further investigations, only the two positively charged dyes, *e.g.* MB and R6G, are taken into consideration.

Blank tests are firstly performed by visible light irradiation of the aqueous dyes solutions in the absence of photocatalyst allowing

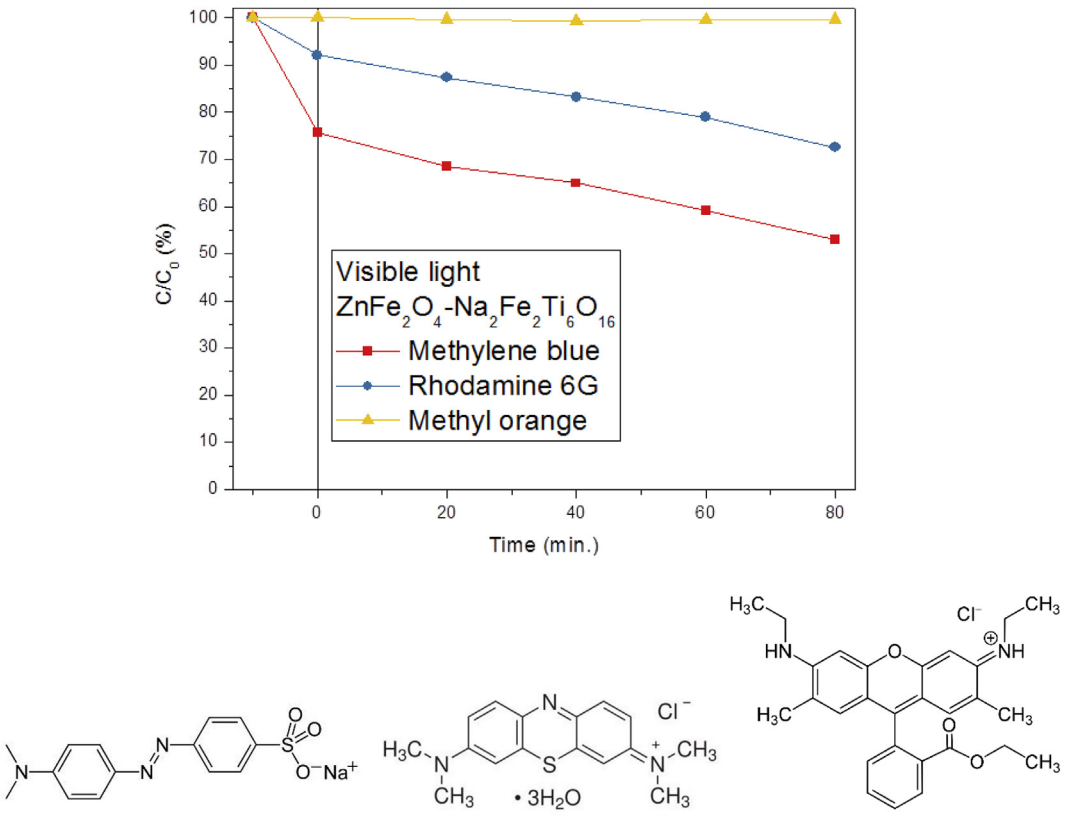

Fig. 8. Degradation of model dyes, namely methylene blue (middle), rhodamine 6G (right) and methyl orange (left) in the presence of $ZnFe_2O_4$—$Na_2Fe_2Ti_6O_{16}$, under visible light irradiation. (For interpretation of the references to colour in this figure legend, the reader is referred to the Web version of this article.)

to conclude that the dyes show high stability under the irradiation conditions. Furthermore, benchmark tests using commercial titania P25 photocatalyst, consisting of roughly 80% anatase and 20% rutile, were performed in order to compare the catalytic efficiency of our newly developed nanocomposite photocatalysts [42]. The results are included in Fig. 9 and show that using the commercial P25 only a small fraction of the dyes was degraded, *e.g.* only 34% of MB and 16% of R6G, respectively. The Ni free catalyst $ZnFe_2O_4$–$Na_2Fe_2Ti_6O_{16}$ managed to degrade both dyes in a percentage of 47% MB and 18% of R6G, respectively, showing a net photocatalytic activity improvement as compared with the commercial P25. This may be well correlated with the enlargement of the photoabsorptive properties of the nanocomposite systems as compared with the titania P25 observed in the UV–Vis DR spectra (Fig. 4). The isomorphous substitution of the Ni^{2+} cations within the spinel structure, further shows a positive effect in the photocatalytic process. The results indicate that the $Zn_{0.4}Ni_{0.6}Fe_2O_4$–$Na_2Fe_2Ti_6O_{16}$ type structure may degrade up to 73% of MB, while the $Zn_{0.8}Ni_{0.2}Fe_2O_4$–$Na_2Fe_2Ti_6O_{16}$ type structure may degrade up to 27% of R6G under the present experimental conditions. It should be noted that the initial concentration is similar (4×10^{-5} M) for both MB and R6G dyes. Therefore, the difference in the maximum degradation efficiency between the two dyes may rely on the higher molecular size and the high abundant benzyl rings present in the R6G molecule as compared with the MB molecule, which makes the R6G more difficult to degrade.

These results indicate that the increase in the photocatalytic efficiency is directly influenced by the shift of the photoabsorptive properties towards the visible region of the solar spectrum, therefore by the band-gap engineering of the newly developed photocatalysts. To further demonstrate these assumptions, the influence of the type of light irradiation, UV, visible or solar light, on the degradation of R6G was investigated for the sample $Zn_{0.8}Ni_{0.2}Fe_2O_4$–$Na_2Fe_2Ti_6O_{16}$ that showed the best photoactivity. As shown in Fig. 10, after the equilibrium was achieved, irradiation with UV light for 80 min leads to a degradation efficiency of only 3% while up to 12% degradation of R6G was achieved under visible light irradiation. The irradiation with solar light, which comprises both UV and visible spectral regions, leads to a total of 25% degradation efficiency. The samples are more active under the visible light than pure TiO_2 and also more active under visible light than under UV light exposure.

The classic photocatalytic materials *e.g.* TiO_2 or ZnO are using only UV light in the degradation process. The successful visible light activation of our developed catalysts represents an important step for its implementation in real wastewater treatment processes. This

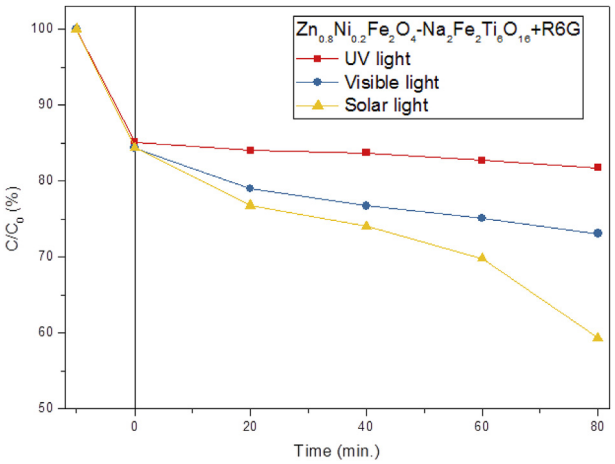

Fig. 10. Degradation of R6G in the presence of $Zn_{0.8}Ni_{0.2}Fe_2O_4$–$Na_2Fe_2Ti_6O_{16}$ under UV, visible and solar light exposure.

has great significance, since the solar light consists of roughly 43% visible light, 53% infrared light and only 4% UV light.

Furthermore, Total organic carbon (TOC) analysis was used to study the photo-mineralization degrees of the MB and R6G after 6 h of illumination under visible light (Fig. 11). The commercial P25 catalyst managed to mineralize only 12% of MB and 3% R6G, respectively. The $ZnFe_2O_4$–$Na_2Fe_2Ti_6O_{16}$ and the Ni^{2+} isomorphously substituted nanocomposites managed to degrade both MB and R6G dyes, in different percentages, showing a net photocatalytic activity improvement as compared with the commercial P25. A general remark is that the mineralization degrees of MB are always higher as compared with the R6G, for the same initial dye concentration, which is in good agreement with the degradation efficiencies measured by UV–Vis spectroscopy, and may be assigned to the difference in molecular size and the number of aromatic rings present in R6G molecules. The best mineralization degree for MB was obtained in the presence of $NiFe_2O_4$–$Na_2Fe_2Ti_6O_{16}$ with 67% of the dye removed. For R6G, 40% was removed by $Zn_{0.4}Ni_{0.6}Fe_2O_4$–$Na_2Fe_2Ti_6O_{16}$.

The schematic proposed mechanism of the photocatalytic process is represented in Fig. 12. The narrow band-gap energy of the Ferrites can be exploited for the photodegradation of the organic pollutants (under visible light). Freudenbergite, as a titanate-type material, is known for good adsorption of methylene blue, but poor photocatalytic activity, results supported also by our

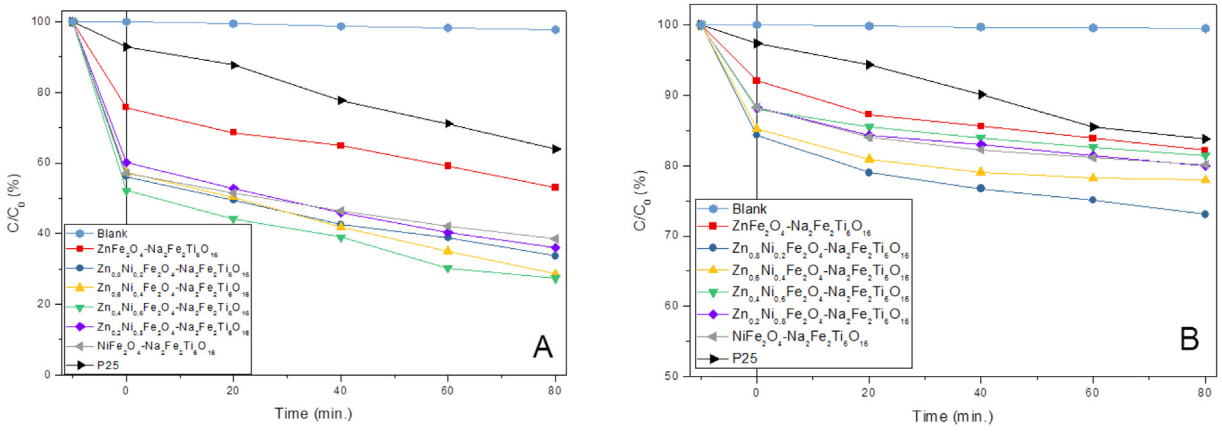

Fig. 9. Degradation study of MB (A) and R6G (B) under visible light irradiation, followed by UV–Vis measurements.

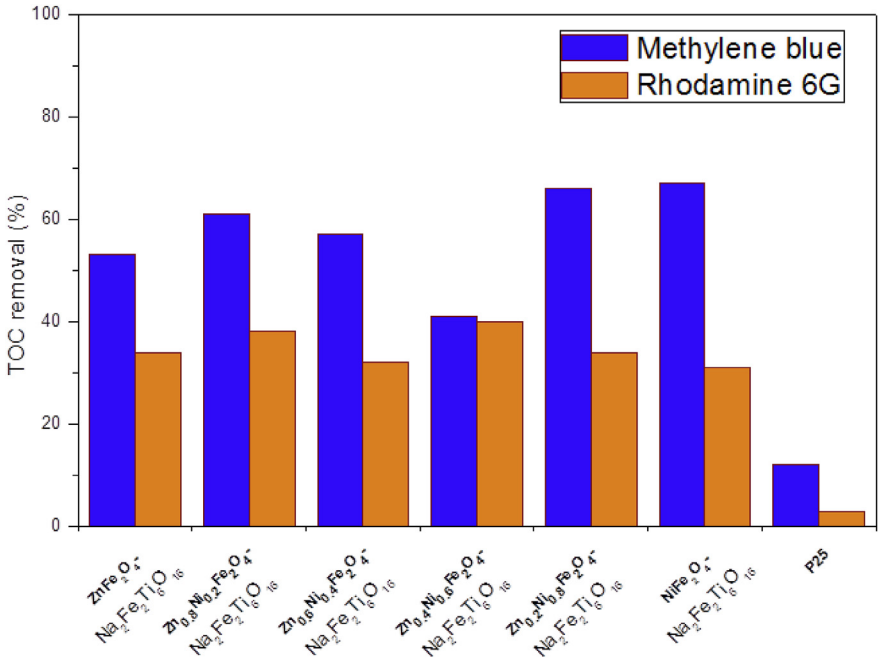

Fig. 11. Degradation study of MB and R6G under visible light irradiation, followed by TOC measurements.

electrochemical analysis performed (not shown) [36]. The visible light energy, is able to promote the electrons from the valence band to the conduction band of $Zn_{1-x}Ni_xFe_2O_4$, forming the e^-—h^+ pairs, which represent the driving force of the photodegradation process. In the first step of the process, the Freudenbergite adsorbs on the surface the positively charged dyes, namely MB and R6G, due to its negatively charged surface in solution. The second step consists of the degradation of the dye molecules in the presence of $Zn_{1-x}Ni_xFe_2O_4$ photocatalyst. This mechanism is supported also by the comparison of the degradation trends followed by MB, R6G and MO in the presence of $ZnFe_2O_4$– $Na_2Fe_2Ti_6O_{16}$. In the case of MO, the only negatively charged dye used in our tests, no interaction with the photocatalyst was observed after the equilibrium time, which led to no degradation in the end (Fig. 8). The enhanced photodegradation properties of Ferrites are due to the well dispersed particles on the surface of Freudenbergite, as evidenced by the AFM images in case of $NiFe_2O_4$– $Na_2Fe_2Ti_6O_{16}$ (Fig. 7 a and b). It can be assumed that the dispersion of the spinel nanoparticles is

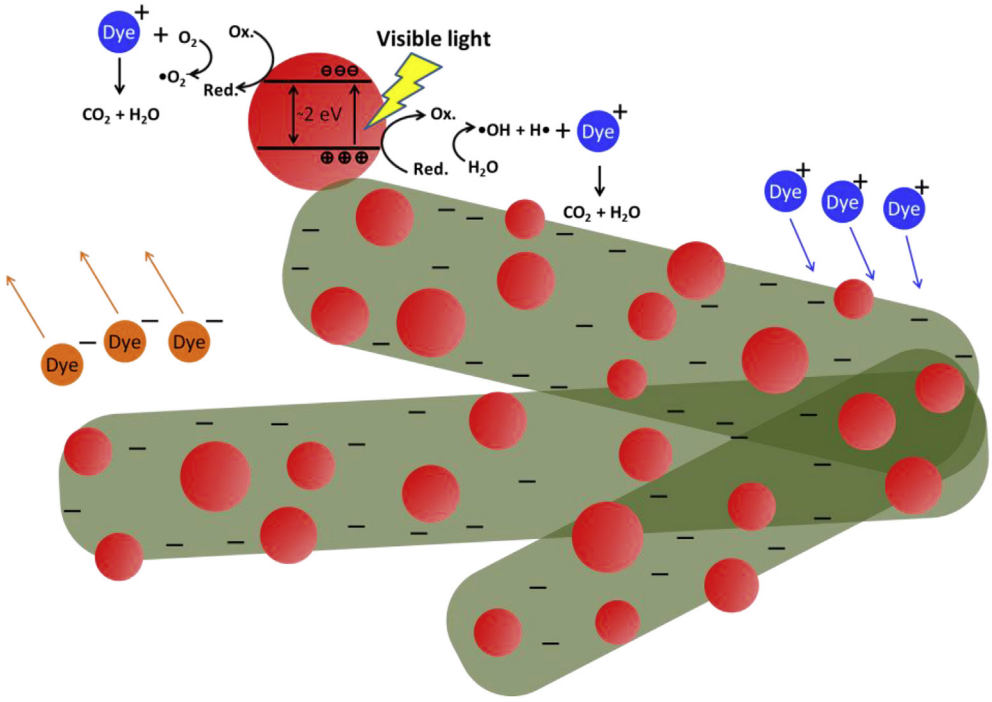

Fig. 12. Schematic representation of the charge separation in the nanocomposites and the proposed photocatalytic degradation mechanism under visible irradiation.

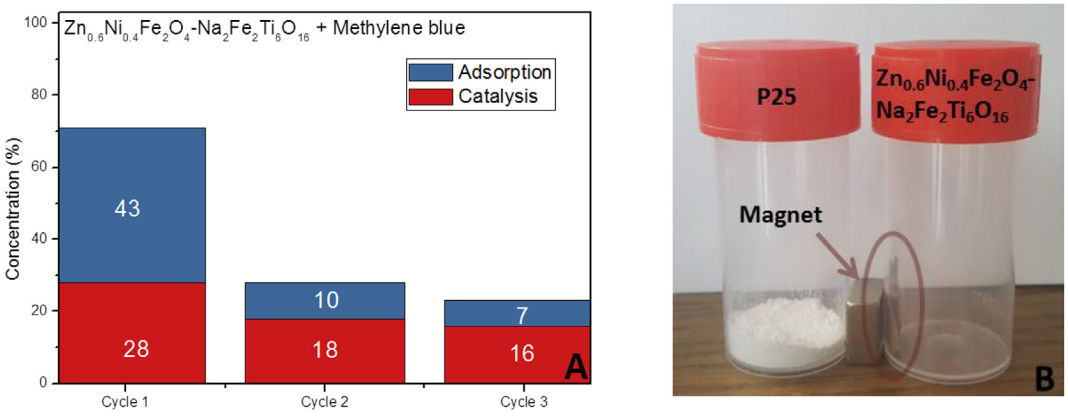

Fig. 13. Degradation of MB in the presence of $Zn_{0.6}Ni_{0.4}Fe_2O_4$–$Na_2Fe_2Ti_6O_{16}$ after 3 cycles of use. Colored in red is the degradation (%) and blue represents adsorption (%) (A). Visually magnetic separation of the catalyst, compared to P25 reference material (B). (For interpretation of the references to colour in this figure legend, the reader is referred to the Web version of this article.)

decreasing the recombination rate of e^-—h^+ pairs. At the same time, the relatively small particles size covers up one of the largest drawbacks of the Ferrites related to the short diffusion length of the charge carriers.

Not to be forgotten that the designed nanocomposites are endowed with magnetic properties as well, which brings further practical advantage for their use in photocatalytic applications. The magnetic properties enable an easy recovery after the end of the process and reuse in a next cycle. The possibility of reusing the recovered photoactive material was also explored in the present study as highlighted in Fig. 13. The degradation of MB dye in the presence of $Zn_{0.6}Ni_{0.4}Fe_2O_4$–$Na_2Fe_2Ti_6O_{16}$ after 3 cycles together with the visually magnetic separation are shown.

After the equilibrium was achieved, a degradation of 28% of MB was observed, compared to 18% and 16% after the second and the third cycles. It should be noted that in the present experimental conditions the photocatalyst has a tendency to stick onto the stirring magnet, therefore not 100% of the solid nanomaterial was used in the next cycle. Moreover, the recyclability study was performed without any regeneration treatment, leading to a decrease in the adsorption of the dye after the equilibrium time between the different cycles. The recyclability of the catalysts would be further explored in order to increase the long term use of the newly developed nanocomposites in photocatalytic wastewater treatment processes.

5. Conclusion

New type of nanocomposites consisting of spinel and Freudenbergite phases were obtained by a two-step synthesis approach and denoted $Zn_{1-x}Ni_xFe_2O_4$–$Na_2Fe_2Ti_6O_{16}$ where x = 0; 0.2; 0.4; 0.6; 0.8; 1. The important roles of the precipitation agent (NaOH) were explained for the formation of both structures. The structural identity was demonstrated by the combination of XRD and Raman characterization, while the morphology of the composite structure was identified by AFM images. Further, TEM analysis clarified the role of the cations in the formation mechanism of the nanocomposite, by revealing the interchange between Ti^{4+} and Fe^{3+} during the formation process. Catalytic performance tests showed that the catalysts can degrade the cationic model dyes (MB, R6G) under visible light irradiation, however they did not show any interaction with the anionic dye (MO). High degradation efficiency was observed when the catalysts were exposed to solar light irradiation, due to the main contribution of the improved activity in visible region of the solar spectrum rather than in the UV spectral region. Furthermore, the photocatalytic capability of the nanocomposites was benchmarked in comparison to the well-known commercial P25 catalyst. All the as-synthetized samples showed higher efficiency for both degradation and mineralization of MB and R6G as compared to P25 under the same reaction conditions. The best catalysts were able to degrade and mineralize 67% of MB and 40% of R6G after 6 h of irradiation with visible light. Finally, the reuse of the catalyst was done successfully, after magnetic separation, in a test of 3 cycles.

Although it is generally known that photocatalysts containing iron have a high recombination rate, we have proven that by following a smart synthetic approach it is possible to overcome this drawback, leading to nanocomposite structures with a better charge separation. The approach followed is a combination of Ferrite spinel, known for having a small band-gap energy, allowing activation under visible light, with Freudenbergite, showing good adsorption properties of the dye molecules. Moreover, the obtained nanocomposites can be smartly removed after the catalytic reaction based on their magnetic properties. The work has resulted in unique nanocomposite photocatalytic materials that are highly active for the degradation of model dyes under visible light.

Author contributions section

Radu-George Ciocarlan: Conceptualization, Methodology, Validation, Formal analysis, Investigation, Writing - Original Draft, Writing - Review & Editing, Visualization, Project administration.

Elena M. Seftel: Conceptualization, Writing - Original Draft, Supervision, Writing - Review & Editing, Funding acquisition.

Raluca Gavrila: Resources, Writing - Original Draft, Writing - Review & Editing.

Mirela Suchea: Resources, Writing - Original Draft, Writing - Review & Editing.

Maria Batuk: Resources, Writing - Original Draft.

Myrjam mertens: Resources.

Joke Hadermann: Resources, Writing - Original Draft.

Pegie Cool: Conceptualization, Resources, Writing - Original Draft, Writing - Review & Editing, Visualization, Supervision, Project administration, Funding acquisition.

Declaration of competing interest

The authors declare that they have no known competing financial interests or personal relationships that could have appeared to influence the work reported in this paper.

Acknowledgements

The authors acknowledge the FWO-Flanders (project nr. G038215N) for financial support.

Appendix A. Supplementary data

Supplementary data to this article can be found online at https://doi.org/10.1016/j.jallcom.2019.153403.

References

[1] V.K. Gupta, et al., Chemical treatment technologies for waste-water recycling-an overview, RSC Adv. 2 (16) (2012) 6380–6388, https://doi.org/10.1039/C2RA20340E.
[2] V. Etacheri, et al., Visible-light activation of TiO2 photocatalysts: advances in theory and experiments, J. Photochem. Photobiol. C Photochem. Rev. 25 (2015) 1–29, https://doi.org/10.1016/j.jphotochemrev.2015.08.003.
[3] M.A. Oturan, J.-J. Aaron, Advanced oxidation processes in water/wastewater treatment: principles and applications. A review, Crit. Rev. Environ. Sci. Technol. 44 (23) (2014) 2577–2641, https://doi.org/10.1080/10643389.2013.829765.
[4] L. Cepoi, et al., Biological methods of wastewater treatment, in: I. Zinicovscaia, L. Cepoi (Eds.), Cyanobacteria for Bioremediation of Wastewaters, Springer International Publishing, Cham, 2016, pp. 45–60.
[5] G.-d. Kang, Y.-m. Cao, Development of antifouling reverse osmosis membranes for water treatment: a review, Water Res. 46 (3) (2012) 584–600, https://doi.org/10.1016/j.watres.2011.11.041.
[6] I. Ali, V.K. Gupta, Advances in water treatment by adsorption technology, Nat. Protoc. 1 (2007) 2661, https://doi.org/10.1038/nprot.2006.370. https://www.nature.com/articles/nprot.2006.370#supplementary-information.
[7] D.H.K. Reddy, Y.-S. Yun, Spinel ferrite magnetic adsorbents: alternative future materials for water purification? Coord. Chem. Rev. 315 (Supplement C) (2016) 90–111, https://doi.org/10.1016/j.ccr.2016.01.012.
[8] L. Zhao, et al., Nanomaterials for treating emerging contaminants in water by adsorption and photocatalysis: systematic review and bibliometric analysis, Sci. Total Environ. 627 (2018) 1253–1263, https://doi.org/10.1016/j.scitotenv.2018.02.006.
[9] S. Gunti, A. Kumar, M.K. Ram, Nanostructured photocatalysis in the visible spectrum for the decontamination of air and water, Int. Mater. Rev. 63 (4) (2018) 257–282, https://doi.org/10.1080/09506608.2017.1379264.
[10] M.R. Hoffmann, et al., Environmental applications of semiconductor photocatalysis, Chem. Rev. 95 (1) (1995) 69–96, https://doi.org/10.1021/cr00033a004.
[11] B. Ohtani, Photocatalysis A to Z—what we know and what we do not know in a scientific sense, J. Photochem. Photobiol. C Photochem. Rev. 11 (4) (2010) 157–178, https://doi.org/10.1016/j.jphotochemrev.2011.02.001.
[12] B. Ohtani, Hidden but possibly fatal misconceptions in photocatalysis studies: a short critical review, Catalysts 6 (12) (2016) 192.
[13] J. Schneider, et al., Understanding TiO2 photocatalysis: mechanisms and materials, Chem. Rev. 114 (19) (2014) 9919–9986, https://doi.org/10.1021/cr5001892.
[14] B. Ohtani, Titania photocatalysis beyond recombination: a critical review, Catalysts 3 (4) (2013) 942.
[15] M. Pelaez, et al., A review on the visible light active titanium dioxide photocatalysts for environmental applications, Appl. Catal. B Environ. 125 (2012) 331–349, https://doi.org/10.1016/j.apcatb.2012.05.036.
[16] P. Vishnukumar, et al., Recent advances and emerging opportunities in phytochemical synthesis of ZnO nanostructures, Mater. Sci. Semicond. Process. 80 (2018) 143–161, https://doi.org/10.1016/j.mssp.2018.01.026.
[17] M. Mishra, D.-M. Chun, α-Fe2O3 as a photocatalytic material: a review, Appl. Catal. Gen. 498 (2015) 126–141, https://doi.org/10.1016/j.apcata.2015.03.023.
[18] X. Wang, H. Fan, P. Ren, Effects of exposed facets on photocatalytic properties of WO3, Adv. Powder Technol. 28 (10) (2017) 2549–2555, https://doi.org/10.1016/j.apt.2017.07.005.
[19] A.M. Al-Hamdi, U. Rinner, M. Sillanpää, Tin dioxide as a photocatalyst for water treatment: a review, Process Saf. Environ. Prot. 107 (2017) 190–205, https://doi.org/10.1016/j.psep.2017.01.022.
[20] B. Paul, et al., Facile synthesis of spinel CuCr2O4 nanoparticles and studies of their photocatalytic activity in degradation of some selected organic dyes, J. Alloy. Comp. 648 (2015) 629–635, https://doi.org/10.1016/j.jallcom.2015.07.012.
[21] K. Lee, et al., Synthesis, optical, and photocatalytic properties of cobalt mixed-metal spinel oxides Co(Al1-xGax)2O4, J. Mater. Chem. 3 (15) (2015) 8115–8122, https://doi.org/10.1039/C4TA06690A.
[22] G. Zhang, et al., Inorganic perovskite photocatalysts for solar energy utilization, Chem. Soc. Rev. 45 (21) (2016) 5951–5984, https://doi.org/10.1039/C5CS00769K.
[23] A. Kubo, G. Giorgi, K. Yamashita, MgTaO2N photocatalysts: perovskite versus ilmenite structure. A theoretical investigation, J. Phys. Chem. C 121 (50) (2017) 27813–27821, https://doi.org/10.1021/acs.jpcc.7b08874.
[24] P.-h. Yuan, et al., Preparation and photocatalytic properties of ilmenite NiTiO3 powders for degradation of humic acid in water, Int. J. Miner. Metall. Mater. 19 (4) (2012) 372–376, https://doi.org/10.1007/s12613-012-0566-6.
[25] E. Casbeer, V.K. Sharma, X.-Z. Li, Synthesis and photocatalytic activity of ferrites under visible light: a review, Separ. Purif. Technol. 87 (2012) 1–14, https://doi.org/10.1016/j.seppur.2011.11.034.
[26] A. Goldman, The magnetization in domains and bulk materials, in: Handbook of Modern Ferromagnetic Materials, Springer US, Boston, MA, 1999, pp. 41–58.
[27] G. Mamba, A. Mishra, Advances in magnetically separable photocatalysts: smart, recyclable materials for water pollution mitigation, Catalysts 6 (6) (2016) 79.
[28] M. Qin, et al., Zinc ferrite composite material with controllable morphology and its applications, Mater. Sci. Eng., B 224 (2017) 125–138, https://doi.org/10.1016/j.mseb.2017.07.016.
[29] H.-Y. Zhu, et al., Novel multifunctional NiFe2O4/ZnO hybrids for dye removal by adsorption, photocatalysis and magnetic separation, Appl. Surf. Sci. 369 (2016) 1–10, https://doi.org/10.1016/j.apsusc.2016.02.025.
[30] A. Ren, et al., Enhanced visible-light-driven photocatalytic activity for antibiotic degradation using magnetic NiFe2O4/Bi2O3 heterostructures, Chem. Eng. J. 258 (2014) 301–308, https://doi.org/10.1016/j.cej.2014.07.071.
[31] H.S. Kim, et al., Synthesis of magnetically separable core@shell structured NiFe2O4@TiO2 nanomaterial and its use for photocatalytic hydrogen production by methanol/water splitting, Chem. Eng. J. 243 (2014) 272–279, https://doi.org/10.1016/j.cej.2013.12.046.
[32] J. Zeng, et al., Plasmonic photocatalyst Au/g-C3N4/NiFe2O4 nanocomposites for enhanced visible-light-driven photocatalytic hydrogen evolution, RSC Adv. 6 (60) (2016) 54964–54975, https://doi.org/10.1039/C6RA08356K.
[33] S.S. Patil, et al., Magnetically separable Ag3PO4/NiFe2O4 composites with enhanced photocatalytic activity, Dalton Trans. 44 (47) (2015) 20426–20434, https://doi.org/10.1039/C5DT03173G.
[34] T. Ishiguro, et al., Freudenbergite, Acta Crystallogr. B 34 (1) (1978) 255–256, https://doi.org/10.1107/S0567740878002708.
[35] A.V. Knyazev, et al., Crystal structure, spectroscopy, and thermal expansion of compounds in MI2O–Al2O3–TiO2 system, J. Solid State Chem. 196 (2012) 110–118, https://doi.org/10.1016/j.jssc.2012.05.043.
[36] Z.-Q. Guo, et al., Novel magnetic semiconductor Na2Fe2Ti6O16: synthesis, double absorption and strong adsorptive ability, J. Mater. Chem. 5 (33) (2017) 17589–17600, https://doi.org/10.1039/C7TA03739B.
[37] A. Jostsons, et al., Immobilization of high level waste in synroc 1 (1988) 537–544.
[38] E.R. Vance, et al., Freudenbergite: a possible synroc phase for sodium-bearing high-level waste, J. Am. Ceram. Soc. 77 (6) (1994) 1576–1580, https://doi.org/10.1111/j.1151-2916.1994.tb09759.x.
[39] R.-G. Ciocarlan, et al., Novel magnetic nanocomposites containing quaternary ferrites systems Co0.5Zn0.25M0.25Fe2O4 (M = Ni, Cu, Mn, Mg) and TiO2-anatase phase as photocatalysts for wastewater remediation under solar light irradiation, Mater. Sci. Eng., B 230 (2018) 1–7, https://doi.org/10.1016/j.mseb.2017.12.030.
[40] D.V. Bavykin, et al., Titanate and Titania Nanotubes: Synthesis, Properties and Applications, RSC Publishing, UK, 2009.
[41] J. Zhang, et al., New understanding of the difference of photocatalytic activity among anatase, rutile and brookite TiO2, Phys. Chem. Chem. Phys. 16 (38) (2014) 20382–20386, https://doi.org/10.1039/C4CP02201G.
[42] S.W. Verbruggen, TiO2 photocatalysis for the degradation of pollutants in gas phase: from morphological design to plasmonic enhancement, J. Photochem. Photobiol. C Photochem. Rev. 24 (2015) 64–82, https://doi.org/10.1016/j.jphotochemrev.2015.07.001.
[43] H.S.C. O'Neill, A. Navrotsky, Simple spinels; crystallographic parameters, cation radii, lattice energies, and cation distribution, Am. Mineral. 68 (1–2) (1983) 181–194.
[44] A. Goldman, Modern Ferrite Technology, Springer, US, 2006.
[45] T. Tatarchuk, et al., Spinel ferrite nanoparticles: synthesis, crystal structure, properties, and perspective applications, in: Nanophysics, Nanomaterials, Interface Studies, and Applications, Springer International Publishing, Cham, 2017.
[46] Bruhn, G. and Knie, Characterization of a Freudenbergite-type Bronze. (vol. 111): p. 4–5.
[47] Bruhn, G. and Knie, Characterization of a Freudenbergite-type Bronze Part 2. (vol. 111): p. 6–7.
[48] G. Bruhn, et al., Low-temperature synthesis of freudenbergite-type titanate bronzes from metal halides, crystal growth from molybdate flux, and crystal structure determination of Na1.84Zn0.92Ti7.08O16, J. Alloy. Comp. 644 (2015) 783–787, https://doi.org/10.1016/j.jallcom.2015.05.076.
[49] J.D. Cashion, et al., Electron hopping in the Mössbauer spectrum of mixed valence freudenbergite, Hyperfine Interact. 226 (1) (2014) 579–583, https://doi.org/10.1007/s10751-013-0964-9.
[50] C. Chen, et al., Synthesis, sintering, transport and thermal properties of Na2Fe2Ti6O16 freudenbergite, Mater. Chem. Phys. 198 (2017) 1–6, https://doi.org/10.1016/j.matchemphys.2017.05.050.
[51] M.N. Akieh, et al., Preparation and characterization of sodium iron titanate ion exchanger and its application in heavy metal removal from waste waters, J. Hazard Mater. 152 (2) (2008) 640–647, https://doi.org/10.1016/j.jhazmat.2007.07.049.
[52] J. Bao, Z. Li, N. Cai, Promoting the reduction reactivity of ilmenite by

introducing foreign ions in chemical looping combustion, Ind. Eng. Chem. Res. 52 (18) (2013) 6119–6128, https://doi.org/10.1021/ie400237p.
[53] R. Shannon, Revised effective ionic radii and systematic studies of interatomic distances in halides and chalcogenides, Acta Crystallogr. A 32 (5) (1976) 751–767, https://doi.org/10.1107/S0567739476001551.
[54] A.L. Patterson, The scherrer formula for X-ray particle size determination, Phys. Rev. 56 (10) (1939) 978–982.
[55] S. Ebraheem, A. El-Saied, Band gap determination from diffuse reflectance measurements of irradiated lead borate glass system doped with TiO_2 by using diffuse reflectance technique, Mater. Sci. Appl. Vol. 04 (No.05) (2013) 6, https://doi.org/10.4236/msa.2013.45042.
[56] M. Thommes, et al., Physisorption of gases, with special reference to the evaluation of surface area and pore size distribution (IUPAC Technical Report), in: Pure and Applied Chemistry, 2015, p. 1051, https://doi.org/10.1515/pac-2014-1117.
[57] Z.Ž. Lazarević, et al., Nanodimensional spinel NiFe2O4 and ZnFe2O4 ferrites prepared by soft mechanochemical synthesis, J. Appl. Phys. 113 (18) (2013) 187221, https://doi.org/10.1063/1.4801962.
[58] M. Hodos, et al., Photosensitization of ion-exchangeable titanate nanotubes by CdS nanoparticles, Chem. Phys. Lett. 399 (4) (2004) 512–515, https://doi.org/10.1016/j.cplett.2004.10.064.
[59] L. Qian, et al., Raman study of titania nanotube by soft chemical process, J. Mol. Struct. 749 (1) (2005) 103–107, https://doi.org/10.1016/j.molstruc.2005.04.002.